

Coherent nanophotonic electron accelerator

<https://doi.org/10.1038/s41586-023-06602-7>

Received: 19 May 2023

Accepted: 31 August 2023

Published online: 18 October 2023

 Check for updates

Tomáš Chlouba^{1,4}, Roy Shiloh^{1,2,4}, Stefanie Kraus^{1,4}, Leon Brückner^{1,4}, Julian Litzel¹ & Peter Hommelhoff^{1,3}

Particle accelerators are essential tools in a variety of areas of industry, science and medicine^{1–4}. Typically, the footprint of these machines starts at a few square metres for medical applications and reaches the size of large research centres. Acceleration of electrons with the help of laser light inside of a photonic nanostructure represents a microscopic alternative with potentially orders-of-magnitude decrease in cost and size^{5–16}. Despite large efforts in research on dielectric laser acceleration^{17,18}, including complex electron phase space control with optical forces^{19–21}, noteworthy energy gains have not been shown so far. Here we demonstrate a scalable nanophotonic electron accelerator that coherently combines particle acceleration and transverse beam confinement, and accelerates and guides electrons over a considerable distance of 500 μm in a just 225-nm-wide channel. We observe a maximum coherent energy gain of 12.3 keV, equalling a substantial 43% energy increase of the initial 28.4 keV to 40.7 keV. We expect this work to lead directly to the advent of nanophotonic accelerators offering high acceleration gradients up to the GeV m^{-1} range utilizing high-damage-threshold dielectric materials²² at minimal size requirements¹⁴. These on-chip particle accelerators will enable transformative applications in medicine, industry, materials research and science^{14,23,24}.

Classical particle accelerators use radio-frequency waves and metallic cavities to accelerate charged particles^{25,26}. The acceleration gradient the particles experience is limited by the radio-frequency peak field that the metallic surfaces can withstand and is typically on the order of dozens of megavolts per metre²⁶. By contrast, dielectric materials can withstand optical fields of 10 GV m^{-1} or more^{12,22,27,28}. Hence, if one could design and fabricate a nanophotonic dielectric structure where the optical nearfields would be synchronized with the charged particles as they propagate, one could achieve an acceleration gradient two-orders-of-magnitude larger than in the radio-frequency case, and thus greatly reduce the size and, as a consequence, the costs of accelerator devices. This is the core idea of the dielectric laser accelerator (DLA)^{12–14,16,21}, also called nanophotonic accelerator.

A proper accelerator not only accelerates particles but also confines them. This way, particle loss is largely mitigated. This confinement is even more important in the case of DLAs because of their submicrometre acceleration channel dimensions. Similar to classical radio-frequency accelerators, a nearfield accelerates the particles, but in a DLA this nearfield is of optical nature. To ensure that the nearfield is strong, the acceleration channel width should equal about one-tenth of the driving wavelength. We choose a width of 225 nm, at a driving wavelength of 1.93 μm . Thus, the length-to-width aspect ratio of our longest accelerator structure (500- μm long) is more than 2,200.

The technique we employ to transversely confine the particles in the nanophotonic acceleration channel is called alternating phase focusing (APF). It circumvents Earnshaw's theorem, which does not allow focusing or collimation of charged particle bunches in

all three dimensions at once, in that it re-focuses the bunched electron beam in one direction while allowing it to defocus in another direction. Slightly later in the structure, the focusing–defocusing roles are reversed, leading to a net confinement and guiding of the bunched particle beam in all three dimensions^{29–31}. We have recently shown that this complex electron phase manipulation technique also works at optical frequencies and at dielectric nanostructures to actively guide an electron beam through a nanometre-wide channel²¹. Here we combine this technique with acceleration to confine the particle bunch and accelerate it in nanofabricated structures up to 500- μm long.

The principle of operation is sketched in Fig. 1. The accelerator nanostructure consists of 2 rows of 2- μm -high silicon pillars (up to 733 pillar pairs; see Fig. 3 and Extended Data Figs. 4 and 5). They generate the required nearfield mode, the exact force components of which we discuss below. To generate this nearfield mode, we illuminate the pillars from the top³² (along the negative y direction) by a beam of laser pulses of 1.93- μm central wavelength and a pulse duration of 250 fs (see Methods for details). The electron beam is injected into the dual pillar structure from the left at an energy of 28.4 keV. The electron beam and the optical nearfield mode travel at the same speed if the synchronicity condition is fulfilled: $\Lambda(z) = \beta(z)\lambda$, where λ is the laser wavelength in vacuum, z is the longitudinal dimension, $\beta(z)$ is the electron velocity normalized to the vacuum speed of light and $\Lambda(z)$ is the local structure period^{12–14,18}. Clearly, for accelerating electrons (increasing $\beta(z)$), the structure period needs to increase^{26,33,34}.

When synchronicity is provided, the synchronous force acting on the electrons is derived from the electric part of the Lorentz force as

¹Physics Department, Friedrich-Alexander-Universität Erlangen-Nürnberg (FAU), Erlangen, Germany. ²Institute of Applied Physics, Hebrew University of Jerusalem (HUJI), Jerusalem, Israel.

³Max Planck Institute for the Science of Light (MPL), Erlangen, Germany. ⁴These authors contributed equally: Tomáš Chlouba, Roy Shiloh, Stefanie Kraus, Leon Brückner. ✉e-mail: tomas.chlouba@fau.de; peter.hommelhoff@fau.de

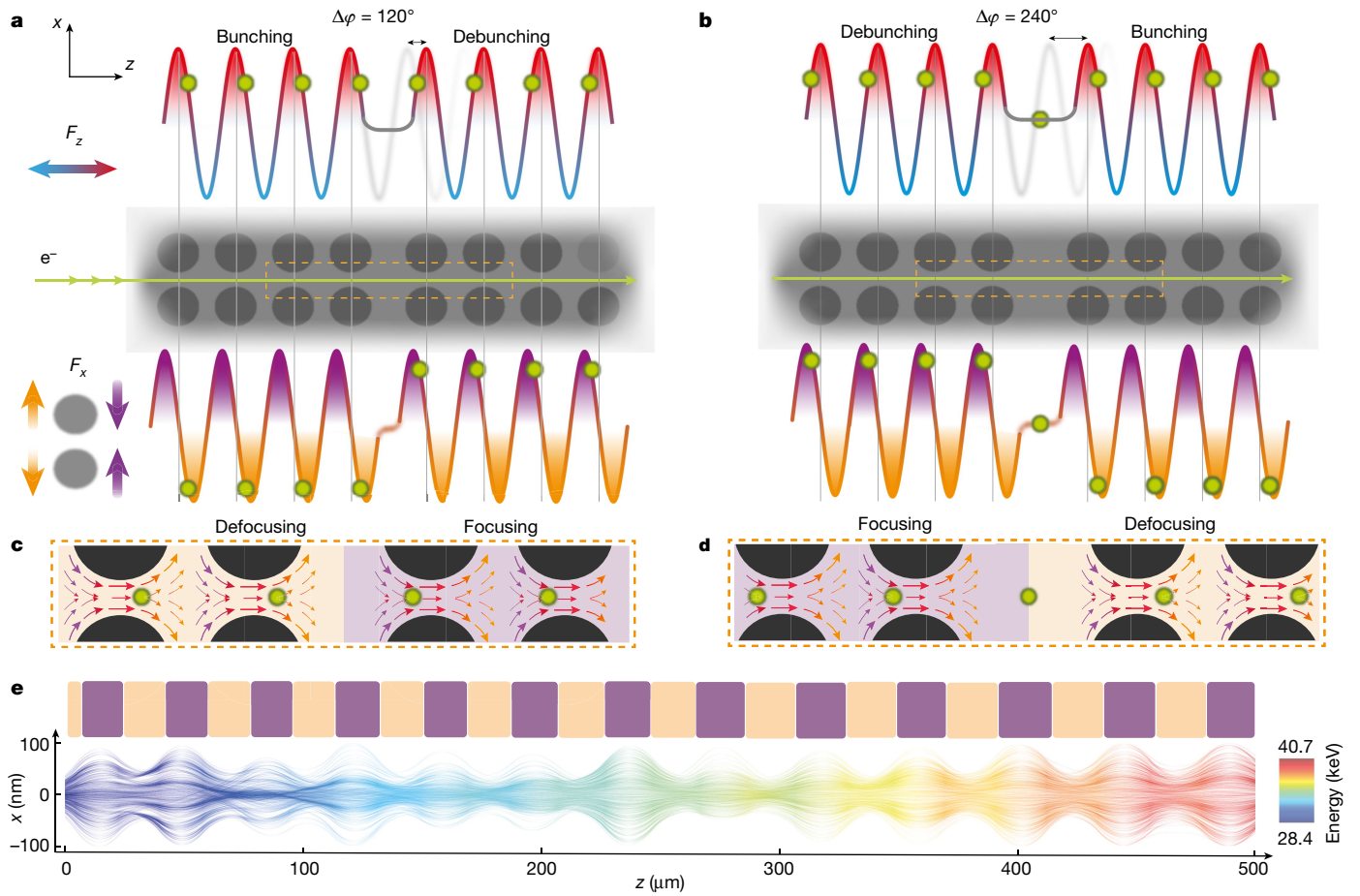


Fig. 1 | Principle of simultaneous acceleration and beam confinement in a nanophotonic structure. **a**, A short, roughly 5- μm -long section of the dual pillar accelerator structure (grey). Laser light incident along the viewing direction generates an optical mode inside of the structure comoving with the electrons (green). Top and bottom: sketches of the synchronous Lorentz force components F_z and F_x acting on a design electron, that is, an electron synchronous with the propagating nearfield mode and initially positioned at a phase of $\varphi_s = 60^\circ$, depicted as a green disk. Before the phase jump, the electron experiences an acceleration force (F_z positive). At the same time, the transverse forces act in a transversally defocusing way on the electrons (F_x negative for electrons at negative x coordinates, for example, see bottom left). After an abrupt phase jump of $\Delta\varphi = 120^\circ$, the electron enters the same nanophotonic mode in the next macrocell, but is now phase-shifted to $\varphi_s = -60^\circ$ (top right).

$$F = \frac{|q|c}{\beta\gamma} A \begin{pmatrix} \frac{1}{\gamma} \sinh(k_x x) \sin \varphi_s \\ 0 \\ \cosh(k_x x) \cos \varphi_s \end{pmatrix}. \quad (1)$$

Here q is the electric charge of the particle, c is the speed of light, γ is the Lorentz factor, A is the excitation coefficient of the synchronous mode, $k_x = 2\pi/(\beta\gamma\lambda)$, and φ_s is the so-called synchronous phase, which we will discuss in detail now.

Figure 1a shows the force components of equation (1) acting on a synchronous electron (green disk) that is slightly below the green centre line and at a synchronous phase of $\varphi_s = 60^\circ$. Clearly, the electron is accelerated in the forward z direction (F_z positive, at 50% of the peak field strength) and it is driven downwards farther away from the centre line (F_x negative). Evidently, this electron will be lost soon if the x component of the force is not flipped. This flipping can be done most elegantly and simply: we introduce a gap into the dual pillar structure,

Also here the electron experiences an acceleration force (positive F_z), but now the transverse forces act in a focusing manner (bottom right; see also c). This repeats with every period of the laser field, that is, every 6.45 fs, which is depicted for multiple laser periods as the electron (green disk) propagates through the structure. The simultaneously arising longitudinal bunching and de-bunching is discussed in the main text. **b**, A depiction of a phase jump from a focusing to a defocusing macrocell with $\Delta\varphi = 240^\circ$ (effectively -120°), shifting the design electron from $\varphi_s = -60^\circ$ to $\varphi_s = 60^\circ$. **c, d**, Zoom-in of the relevant regions in **a** and **b**, respectively, with the arrows showing the force field at one instant in time. **e**, Simulated trajectories of electrons as they travel through the accelerator structure while gaining energy (colour shows instantaneous energy). The orange and purple blocks above depict the corresponding macrocells that act transversally focusing (purple) and defocusing (orange).

which basically allows us to generate a new optical nearfield mode, only phase-shifted to the previous one. Because the electron moves at roughly constant speed, after this gap it enters the synchronous mode at a different phase. We choose the gap size such that the electron undergoes a 120° phase jump ($\Delta\varphi$); hence, now it experiences the forces for $\varphi_s = -60^\circ$. That is, the force still acts accelerating, but now the x direction acts to re-focus the electron towards the central axis (F_x now positive; see bottom of Fig. 1a).

Following Earnshaw's theorem, the focusing in the x direction has to lead to defocusing in another dimension. In this case, this is the longitudinal coordinate z (or s in the frame comoving with the electron). Before the phase jump (at $\varphi_s = 60^\circ$), where the electron experiences acceleration forces (F_z positive), the slope dF_z/dz is negative (more precisely dF_s/ds is negative, where s is the longitudinal dimension in the frame comoving with the design electron), exerting a force that longitudinally focuses the electron around the design phase leading to bunching. After the phase jump (at $\varphi_s = -60^\circ$), the role reverses: the longitudinal force F_z is still positive and accelerating, however, the

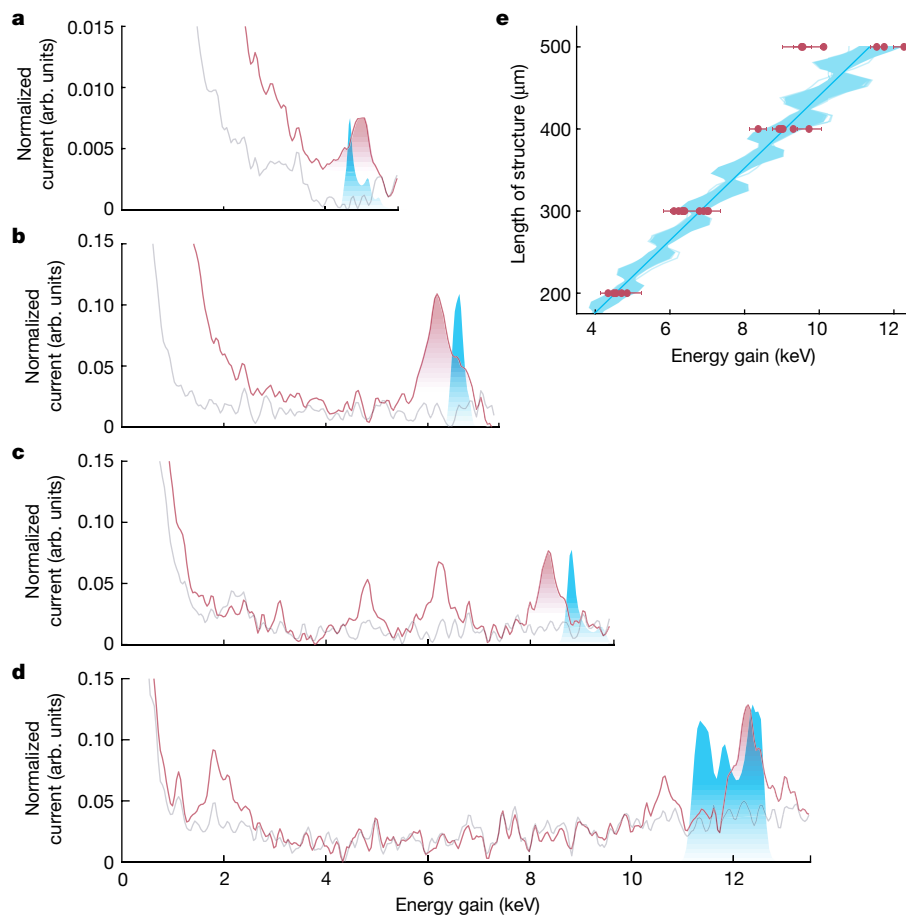


Fig. 2 | Electron energy spectra showing coherent electron acceleration.

a–d, Electron energy spectra (red) recorded from electrons having passed nanophotonic acceleration structures of 200 μm (**a**), 300 μm (**b**), 400 μm (**c**) and 500 μm (**d**) length, all driven with an optical field strength of around 600 MV m⁻¹. We observe coherent electron acceleration for all four structures: a clear peak in the energy spectrum, highlighted with red shading, at the position expected from the design acceleration gradient of 22.7 MeV m⁻¹. The numerical simulation results are shown in light blue, matching the measured coherent acceleration peak well. Each spectrum is normalized to the zero-loss peak height without any laser illumination (grey). See text for details. **e**, From

various more spectra like the ones shown in **a–d**, we extract the energy of the coherent acceleration peak, and plot it versus the structure length (red dots). The values scatter mainly because of slight drifts in the driving laser field strength. The error bars are the standard deviations of the Gaussian fits to the coherent acceleration peaks. The graph also shows the average gradient design curve (blue line) and particle trajectories (light blue band of curves; see text and Methods for details). We note that the oscillations in energy around the design curve result from an interplay between the electron distribution and structure design (see Methods).

slope is positive leading to debunching and extending of the electron pulse in time (and phase).

After this, we introduce another phase jump, now of $\Delta\phi = 240^\circ$, to bring the design electron back to the original force components (Fig. 1b,d). This works because the maxima of the transverse force F_x are phase-shifted relative to the maximum acceleration phase, $\phi_s = 0^\circ$, by 90° . Hence, we see that all vector components of equation (1) are of highest interest as they allow acceleration and beam confinement in a combined fashion. The structure then represents what is called a FODO lattice, where F and D stand for focusing and defocusing and O stands for drift, which in our case happens to be in the APF gaps ($\Delta\phi$ phase jumps)^{26,30}.

By concatenating identical macrocells with repeated $\Delta\phi = 180^\circ$ phase jumps, we recently showed active transport of electrons through a pure transport structure, that is, without acceleration²¹. Hence, we showed that stable electron trajectories can be attained within the acceleration channel. In the work presented here, we go a large step further. We now combine alternating phase focusing (with 120° and 240° phase jumps) with specially designed tapered structure geometries to facilitate the combination of nanophotonic coherent acceleration and collimation of a pulsed electron beam. We use up to 25 gaps, separating up to

26 accelerator macrocells from each other, each macrocell being different from every other because of the increasing particle velocity. Design and clean-room fabrication of such structures are much more intricate and demanding than pure APF transport structures (see Methods for details). In the following, we show structures that provide acceleration in combination with the just-discussed two-dimensional alternating phase focusing (collimation forces along x and z). Three-dimensional alternating phase focusing can be realized with more complex structures³¹, which is not required here.

To obtain a concrete design of a working DLA structure based on the above, we solve for the optical nearfields in the photonic nanostructure numerically³⁵ and export these fields into a particle-tracking code to perform trajectory simulations³⁶. As our laser pulses are shorter than the electron pulse (250 fs versus 700 fs full-width at half-maximum (FWHM)), many electrons do not interact with the peak of the designed acceleration field or quickly fall out of synchronicity with the tapered design of the structure period. We therefore conservatively chose our structure to follow an average acceleration gradient of 22.7 MeV m⁻¹, at $\phi_s = 60^\circ$ off-crest at the injection energy. We note that the number of electrons captured in phase space and accelerated is larger when operating away from the crest, at the price of a reduced acceleration

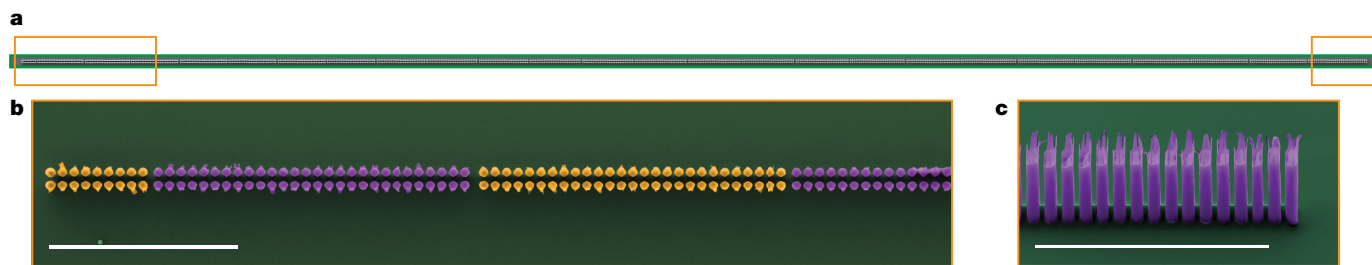


Fig. 3 | Nanophotonic accelerator structure. **a**, Coloured scanning electron microscope image of the entire 0.5-mm-long structure. The electrons are injected from the left side. **b**, Top view of the initial part of the accelerator showing individual pillars and the guiding channel. Purple pillars form

(transversally) focusing macrocells and the orange pillars form (transversally) defocusing macrocells. **c**, Side view of the last macrocell of the accelerator. Scale bars in **b** and **c**, 10 μm .

gradient. The positions and sizes of the APF phase jumps are first chosen from theory³⁰ to maximize the throughput of electrons through the structure, and then numerically adjusted according to the growing energy of the electrons (see Methods for details).

To demonstrate acceleration in combination with alternating phase focusing, we have fabricated a number of structures of the same design and with various lengths, ranging from 200 μm to 500 μm (Fig. 3). This way, we can track the acceleration and collimation behaviour in separate stages of the accelerator.

Figure 2a–d shows the results for structures 200 μm , 300 μm , 400 μm and 500 μm long. We observe average energy gains of 4.59 ± 0.29 keV, 6.57 ± 0.32 keV, 9.05 ± 0.24 keV and 10.8 ± 0.29 keV, respectively. These are matched well by our simulations, which yield 4.5 keV, 6.6 keV, 8.8 keV and 11.9 keV, respectively (see also Fig. 2e and Methods). The averages are over measurements of different structures of the same design where some structures might be imperfect due to fabrication errors. The acceleration in the best of the 500- μm -long structures boosts electrons from 28.4 keV all the way to 40.7 keV, representing a substantial 43% increase of the start energy. In all cases, the rather narrow peak of accelerated electrons is matched by simulation results and clearly shows that we have achieved coherent acceleration of electrons in combination with alternating phase focusing. We note that similar results have been reported in ref. 37. We measure roughly one accelerated electron per second (Methods). Importantly, the electron number in the coherent acceleration peak hardly changes with increasing structure length. Like in classical radio-frequency accelerators, although now at driving frequencies a factor of about 10,000 higher and similarly smaller acceleration structures, we may now speak of coherent ‘buckets’ of electrons being accelerated and kept together by the synchronous optical forces, with their control knobs built into the nanophotonic structure. Although not used here, one may tune the accelerator sections independently with the help of a spatial light modulator tuning the driving pulses³⁸.

In addition to the clear coherent acceleration peak just discussed, we see that the zero-loss peak is still present in all measurements (Extended Data Fig. 6). This is again mainly because the electron pulses are longer than the laser pulses. Furthermore, we see an energy modulation, that is, acceleration and deceleration, around the zero-loss peak. These electrons reach some energy (gain or loss) and then fall out of synchronicity. From this point on, they just oscillate around the energy they had when they fell out of synchronicity as matched by our simulation results (see Methods for details, Extended Data Fig. 2 and Supplementary Videos 1 and 2).

We detect electrons also between the coherent acceleration peak and zero energy gain (Fig. 2b–d). These electrons are only partly accelerated: they have been captured by the acceleration bucket but were lost at some point, thus losing synchronicity. This may happen to electrons close to the separatrix²⁵, but also technical reasons contribute such as the laser pulse front tilt being linear and thus not perfectly matched

to the increasing electron velocity (see Methods, Extended Data Fig. 1 and Supplementary Video 2).

Our nanophotonic accelerators were designed to show an average gradient of 22.7 MeV m^{-1} , clearly much below GeV m^{-1} acceleration gradients, but already on par with today’s radio-frequency accelerator gradients for relativistic electrons³⁹. The current gradient in this proof-of-concept work is not larger for various reasons, including the non-relativistic nature of the electrons making it hard to excite the synchronous nanophotonic mode efficiently, the rather conservative choice of the design phase (50% off-crest gradient), the fact that we worked with constant pillar diameters, and, more generally, a not at all fully optimized choice of nearfield excitation structure design. Now that the nanophotonic particle accelerator is demonstrated, the next steps will be to further improve the structure design and systematically work towards GeV m^{-1} acceleration gradients, in combination with targeting larger currents. We note that a gradient of 1.8 GeV m^{-1} has been demonstrated with relativistic electrons²². In addition, higher laser repetition rates will lead to a larger beam current, which can be also achieved by a much more intriguing possibility resulting from nanofabrication: many accelerator channels can be fabricated next to each other, all driven with the same laser field⁴⁰, possibly even in three dimensions⁴¹. Importantly, we expect that future nanophotonic accelerators will employ the same design principles as demonstrated here. Although the technical challenges are large and considerable work still needs to be done to bring nanophotonic accelerators to applications, we expect our work to result in novel compact light sources⁴², compact free electron lasers^{14,43} and possibly even high-energy colliders²³. Particularly attractive nearer-term applications might include a catheterized accelerator-on-a-chip-based radiation source for radiation therapy¹⁴ or a research accelerator with an on-purpose limited electron current for searches of light dark matter^{44,45}.

Online content

Any methods, additional references, Nature Portfolio reporting summaries, source data, extended data, supplementary information, acknowledgements, peer review information; details of author contributions and competing interests; and statements of data and code availability are available at <https://doi.org/10.1038/s41586-023-06602-7>.

- Karzmark, C. J. Advances in linear accelerator design for radiotherapy. *Med. Phys.* **11**, 105–128 (1984).
- Podgorsak, E. B. *Radiation Oncology Physics: A Handbook for Teachers and Students* (International Atomic Energy Agency, 2005).
- Bucksbaum, P., Möller, T. & Ueda, K. Frontiers of free-electron laser science. *J. Phys. B* **46**, 160201 (2013).
- Focus: synchrotron techniques. *Nat. Rev. Mater.* <https://www.nature.com/collections/vjzmtcbvzy> (2018).
- Shimoda, K. Proposal for an electron accelerator using an optical maser. *Appl. Opt.* **1**, 33 (1962).

6. Lohmann, A. Electron acceleration by light waves. *IBM Tech. Note* **5**, 169–182 (1962).
7. Takeda, Y. & Matsui, I. Laser linac with grating. *Nucl. Instrum. Methods* **62**, 306–310 (1968).
8. Mizuno, K., Pae, J., Nozokido, T. & Furuya, K. Experimental evidence of the inverse Smith–Purcell effect. *Nature* **328**, 45–47 (1987).
9. Rosenzweig, J., Murokh, A. & Pellegrini, C. A proposed dielectric-loaded resonant laser accelerator. *Phys. Rev. Lett.* **74**, 2467–2470 (1995).
10. Huang, Y. C., Zheng, D., Tulloch, W. M. & Byer, R. L. Proposed structure for a crossed-laser beam, GeV per meter gradient, vacuum electron linear accelerator. *Appl. Phys. Lett.* **68**, 753–755 (1996).
11. Plettner, T. et al. Visible-laser acceleration of relativistic electrons in a semi-infinite vacuum. *Phys. Rev. Lett.* **95**, 134801 (2005).
12. Peralta, E. A. et al. Demonstration of electron acceleration in a laser-driven dielectric microstructure. *Nature* **503**, 91–94 (2013).
13. Breuer, J. & Hommelhoff, P. Laser-based acceleration of nonrelativistic electrons at a dielectric structure. *Phys. Rev. Lett.* **111**, 134803 (2013).
14. England, R. J. et al. Dielectric laser accelerators. *Rev. Mod. Phys.* **86**, 1337–1389 (2014).
15. Leedle, K. J. et al. Dielectric laser acceleration of sub-100 keV electrons with silicon dual-pillar grating structures. *Opt. Lett.* **40**, 4344 (2015).
16. Sapra, N. V. et al. On-chip integrated laser-driven particle accelerator. *Science* **367**, 79–83 (2020).
17. Niedermayer, U. et al. Challenges in simulating beam dynamics of dielectric laser acceleration. *Int. J. Mod. Phys. A* **34**, 1942031 (2019).
18. Shiloh, R. et al. Miniature light-driven nanophotonic electron acceleration and control. *Adv. Opt. Photon.* **14**, 862 (2022).
19. Black, D. S. et al. Net acceleration and direct measurement of attosecond electron pulses in a silicon dielectric laser accelerator. *Phys. Rev. Lett.* **123**, 264802 (2019).
20. Schönenberger, N. et al. Generation and characterization of attosecond microbunched electron pulse trains via dielectric laser acceleration. *Phys. Rev. Lett.* **123**, 264803 (2019).
21. Shiloh, R. et al. Electron phase-space control in photonic chip-based particle acceleration. *Nature* **597**, 498–502 (2021).
22. Cesar, D. et al. High-field nonlinear optical response and phase control in a dielectric laser accelerator. *Commun. Phys.* **1**, 46 (2018).
23. Shiltsev, V. & Zimmermann, F. Modern and future colliders. *Rev. Mod. Phys.* **93**, 015006 (2021).
24. Hermann, B. et al. Inverse-designed narrowband THz radiator for ultrarelativistic electrons. *ACS Photon.* **9**, 1143–1149 (2022).
25. Wangler, T. *RF Linear Accelerators* (Wiley-VCH, 2008).
26. Chao, A. W., Mess, K. H., Tigner, M. & Zimmermann, F. *Handbook of Accelerator Physics and Engineering* (World Scientific, 2013); <https://doi.org/10.1142/8543>.
27. Tien, A.-C., Backus, S., Kapteyn, H., Murnane, M. & Mourou, G. Short-pulse laser damage in transparent materials as a function of pulse duration. *Phys. Rev. Lett.* **82**, 3883–3886 (1999).
28. Soong, K., Byer, R. L., Colby, E. R., England, R. J. & Peralta, E. A. Laser damage threshold measurements of optical materials for direct laser accelerators. *AIP Conf. Proc.* **1507**, 511–515 (2012).
29. Courant, E. & Snyder, H. Theory of the alternating-gradient synchrotron. *Ann. Phys.* **3**, 1–48 (1958).
30. Niedermayer, U., Egenolf, T., Boine-Frankenheim, O. & Hommelhoff, P. Alternating-phase focusing for dielectric-laser acceleration. *Phys. Rev. Lett.* **121**, 214801 (2018).
31. Niedermayer, U., Egenolf, T. & Boine-Frankenheim, O. Three dimensional alternating-phase focusing for dielectric-laser electron accelerators. *Phys. Rev. Lett.* **125**, 164801 (2020).
32. Shiloh, R., Chlouba, T., Yousefi, P. & Hommelhoff, P. Particle acceleration using top-illuminated nanophotonic dielectric structures. *Opt. Express* **29**, 14403 (2021).
33. McNeur, J. et al. Elements of a dielectric laser accelerator. *Optica* **5**, 687 (2018).
34. Wideröe, R. Über ein neues Prinzip zur Herstellung hoher Spannungen. *Arch. Elektrotechnik* **21**, 387–406 (1928).
35. Ansys Lumerical <http://www.lumerical.com/> (2019).
36. de Loos, M. J. & van der Geer, S. B. General Particle Tracer: a new 3D code for accelerator and beamline design <http://www.pulsar.nl/gpt/> (2001).
37. Broadus, P. et al. Sub-relativistic alternating phase focusing dielectric laser accelerators. Preprint at <https://arxiv.org/abs/2310.02434> (2023).
38. Ody, A., Crisp, S., Musumeci, P., Cesar, D. & England, R. J. SHaRD: a beam dynamics simulation code for dielectric laser accelerators based on spatial harmonic field expansion. *Nucl. Instrum. Methods Phys. Res. Sect. A* **1013**, 165635 (2021).
39. Wuensch, W. High-gradient breakdown in normal-conducting RF cavities. *Proc. European Particle Accelerator Conference* 134–138 (2002).
40. Zhao, Z. et al. Design of a multichannel photonic crystal dielectric laser accelerator. *Photon. Res.* **8**, 1586 (2020).
41. Staude, I. et al. Waveguides in three-dimensional photonic bandgap materials for particle-accelerator on a chip architectures. *Opt. Express* **20**, 5607 (2012).
42. Roques-Carmes, C. et al. Towards integrated tunable all-silicon free-electron light sources. *Nat. Commun.* **10**, 3176 (2019).
43. Naranjo, B., Valloni, A., Putterman, S. & Rosenzweig, J. B. Stable charged-particle acceleration and focusing in a laser accelerator using spatial harmonics. *Phys. Rev. Lett.* **109**, 164803 (2012).
44. Åkesson, T. et al. Light Dark Matter Experiment (LDMX). Preprint at <https://arxiv.org/abs/1808.05219> (2018).
45. Markiewicz, T. et al. The SLAC Linac to ESA (LESA) beamline for dark sector searches and test beams. Preprint at <https://arxiv.org/abs/2205.13215> (2022).

Publisher's note Springer Nature remains neutral with regard to jurisdictional claims in published maps and institutional affiliations.

Springer Nature or its licensor (e.g. a society or other partner) holds exclusive rights to this article under a publishing agreement with the author(s) or other rightsholder(s); author self-archiving of the accepted manuscript version of this article is solely governed by the terms of such publishing agreement and applicable law.

© The Author(s), under exclusive licence to Springer Nature Limited 2023

Methods

Overview of the experimental set-up

The driving laser is an ytterbium fibre laser at a wavelength of 1,030 nm with a pulse duration of 250 fs and a repetition rate of 167 kHz, generating laser pulses with an energy of 600 μJ . It pumps an optical parametric amplifier to generate infrared laser pulses with a wavelength of 1.93 μm and with up to 60 μJ of pulse energy. A part of the pump beam is split off to generate 257-nm ultraviolet pulses through fourth-harmonic generation. This light is used to trigger photoemission from the electron source (Extended Data Fig. 1). The infrared pulses at 1.93 μm are pulse-front-tilted to generate the required 71° of pulse-front-tilt angle for optical overlap of the moving electrons and the laser pulses (see details of the pulse-front-tilt set-up below). The other beam direction (in the x direction) is focused with a 20-mm-focal-length cylindrical aspheric lens onto the nanophotonic structure. This way, we achieve a highly elongated focal spot on the nanostructure with a spot radius of 640 μm ($1/e^2$ intensity) along the z direction and 13 μm in the x direction. The laser polarization is linear along the electron propagation direction (z direction). To generate the design optical field strength of 600 MV m^{-1} , the pulse energy equals 2.2 μJ and the average power is 360 mW (fluence of 16.5 mJ cm^{-2}). Our silicon nanostructures have survived without visual damage all the way to roughly 460 mW (fluence of 21 mJ cm^{-2}). For our structures, the design optical field strength of 600 MV m^{-1} translates into an average acceleration gradient of 22.7 MeV m^{-1} .

The electron source in the experiment is a modified commercial scanning electron microscope (SEM; Philips XL30). The ultraviolet laser pulses are focused onto the Schottky tip cathode of the SEM with a pulse energy of 4 nJ to generate electron pulses through photoemission. The electrons are accelerated to a beam energy of 28.4 keV in the microscope column. They are focused into the accelerator structure, which is mounted in the sample chamber of the SEM at a distance roughly 3 cm away from the exit of the SEM's final focus lens. The electron pulse length at the structure is about 700 fs FWHM. The temporal overlap between the electron pulses and the infrared laser pulses is set using a motorized delay stage. The electron energy spectrum is measured with a home-built magnetic spectrometer and is read out via the phosphor screen of a microchannel plate detector and a camera. More details are given in ref. 46.

To feed the electron beam into the accelerator structure and to align the accelerator structure parallel to the electron beam, initial alignment is performed based on imaging via conventional SEM imaging of the structure in Schottky emission mode (no ultraviolet laser triggering): the horizontal and vertical angle (relative to the electron propagation direction) of the structure is set with the help of alignment apertures at both ends of the channel. Then the electron beam is focused to the entrance of the accelerator structure, that is, the plane of the first pair of pillars, at roughly two-thirds of the pillar height so that an enhancement of the transmitted current due to the APF guiding is observed. The laser alignment is found by imaging the reflection from the chip surface.

Pulse-front-tilt set-up and measurement

A grating with 600 grooves per mm with a blaze angle of 34° at 1,850 nm is used to generate the pulse front tilt with a final angle of $\alpha = 71^\circ$ for an optimal electron and laser pulse overlap. The angle of 71° is matched to an electron speed of $v = c/\tan(71^\circ) = 0.344c$, corresponding to an energy of 33.2 keV, representing a compromise between initial and final electron energies. The angle of incidence with respect to the grating normal is 29° and the angle of the first-order diffracted beam is 42° . The grating is imaged onto the nanophotonic structure using a cylindrical zoom lens system. The zoom lens consists of four cylindrical lenses with focal lengths $f_1 = f_4 = 300$ mm and $f_2 = f_3 = 100$ mm. The zoom lens system provides independent control over image distance and magnification. The magnification adjusts the inclination angle of the

pulse front and the size of the laser beam on the structure. To measure the pulse-front-tilt angle, we built an auxiliary set-up, which is accessible via a flip mirror⁴⁷ (not shown). We measure $\alpha = -(71 \pm 1.8)^\circ$ after the zoom lens. This pulse-front-tilt angle depends on the magnification of the zoom lens system, which we set to $M = 0.5$.

Structure design and optimization

The full Lorentz force acting on an electron at any one time is complex and its amplitude is generally five to ten times stronger than the force exerted just by the synchronous mode (equation (1)). However, most of this force will average out over a laser period and mainly the synchronous force has a net effect on the electron. Still, the full force cannot be completely disregarded because the electron motion has to be accurately tracked. Hence, in our numerical simulations we take the full Lorentz force into account, including the magnetic-field component, with high resolution, rather than solving the whole structure design purely with an analytical approach based on equation (1).

The electromagnetic fields inside of the nanophotonic accelerator were solved in two dimensions using the Ansys Lumerical finite difference time domain software. Field maps were imported into General Particle Tracer to perform particle-tracking simulations. We disregarded any changes of the electromagnetic fields in the y direction (normal to the substrate). For the structure design, the electron and laser beam parameters were chosen specifically to be optimal and ideal: the laser is modelled as a continuous-wave single-frequency 1.93- μm -wavelength plane-wave, and the electron pulse is spatially on-axis and assumed uniformly distributed in time over one optical cycle, 6.45 fs, with zero emittance and monoenergetic at 28.4 keV. The ideality of the design parameters is advantageous solely for the optimization process, where otherwise optimizing the structure design to non-ideal beams could make the experiment more difficult: the basic assumption is that the beam in the experiment is prepared to tend towards these ideal conditions.

The optimization process attempts to fit the energy gain as a function of propagation distance in the structure to a predefined energy gain curve. A conservative design curve was chosen, with an injection angle of 60° off-crest ($\phi_s = 60^\circ$ in equation (1)), yielding a design gradient of 22.7 MeV m^{-1} with an incident laser field strength of 600 MV m^{-1} . (To prevent potential confusion, we note that we define ϕ_s as the synchronous phase with the crest set at 0° rather than 180° as done in various text books.) We note that excluding the injection phase, the phase accumulation of the particle between APF phase jumps is not explicitly optimized in the design process; rather, the algorithm attempts to follow the energy gain design curve as much as possible. This results in a phase curve that would follow the ideal description in the main text to some extent, but deviates in that the phase jumps would vary throughout the structure. One reason we pursued this optimization approach lies in the nature of the phase jumps themselves: while in theory these jumps are sharp and immediate, in practice the effect of the discontinuity in the tapered structure affects the nearby periods, up to roughly one wavelength. This in turn alters the accumulated phase slightly, but eventually substantially over long structures. Other approaches can be chosen to follow both the energy gain design curve and phase jump methodology as described in the main text. We expect inverse design methods to provide close-to-optimal structures soon^{16,48}.

In our structure design optimization, each design round has three steps: first, the electromagnetic fields are solved, then particles are tracked through the fields, and finally the results are analysed and fed to the next optimization round. Although higher nearfields can be achieved at higher electron energies (and thereby higher acceleration gradients) by changing the pillar geometry along the structure, we chose to keep the geometry constant: the pillars are elliptic with radii of 240 nm \times 225 nm (longitudinal \times transverse). This is practically advantageous to the fabrication process, which would otherwise require additional optimization and fine-tuning to accommodate the varying pillar

sizes during etching. The pillars are situated symmetrically around a 225-nm-wide acceleration channel gap, through which the electrons propagate. Overall, there are two design parameters: the local structure period and the position of the APF phase jumps. The tapering of the structure period throughout the structure length is adjusted to match the synchronicity condition based on the particle-tracking results through the fields. This, along with the position and size of the APF phase jumps, is calculated numerically in each optimization round from theory³⁰.

As previously mentioned, the optimization algorithm is designed such that all phases are initially injected to the structure. However, principally, the design parameters are based on the results of one single electron that matches best (using a least-squares fit) to the average gradient design curve. In each step, the algorithm attempts to use the same particle chosen in the previous step; however, if the particle falls completely off synchronicity, the algorithm chooses the next best one, which is necessarily close and within the injection phase error of the initially chosen particle, thereby working around some numerical discretization issues. As a result, the final structure design is obtained with a single design particle that is not lost and best matches the design curve.

The simulations are run on a Windows 10 AMD EPYC 7542 equipped with two 32-core processors. The field-solving and particle-tracking steps take roughly 8 min, using about 40 GB of random-access memory with a rectangular mesh size of 9 nm per cell and recording a single wavelength in the finite difference time domain simulation. Two thousand particles are tracked in the design process, giving a resolution of 3.2 as or 0.18° in the injection phase.

Extended Data Figs. 2 and 3 depict the results of the structure design step, in both energy gain and transverse dynamics, respectively. As previously mentioned, although here the injected beam is uniformly distributed with a full width of 20 nm around the optical axis, it is otherwise ideal: zero emittance and zero initial energy spread, uniformly spans all phases, and is injected with an energy of 28.4 keV. Under these conditions, the simulation predicts (green curve in Extended Data Fig. 3) that 1,100 particles out of 30,000 are captured and accelerated towards the output of the structure, or a bandwidth of 3.66% of all injected phases. In Extended Data Fig. 3, the envelope of the accelerated electrons appears to grow throughout the structure, but is, however, still contained and confined within the acceleration channel boundaries. Nevertheless, the optimization algorithm can be designed to additionally optimize this envelope and confine it further. Additional information is given in the captions.

Supplementary Video 1 shows the transverse positions of the electrons versus the z axis in the laboratory frame, and the evolution of the captured electrons from the injection energy (28.4 keV, blue) towards full energy gain (over 40 keV, red). The captured electrons show a ‘breathing’ motion, focusing and defocusing, as expected from the APF theory. Also evident is the zero-loss peak and uncaptured electrons, which start to lag behind and eventually spatially separate from the captured and accelerated electrons. These electrons still oscillate in space and energy because they are unsynchronized with the structure, but also because of the action of the APF phase jumps.

Supplementary Video 2 depicts a complementary view of the nanophotonic action on the electrons in phase space: it follows the energy gain of the captured electrons versus the z axis in a comoving frame around the best-matching electron (black disk). After roughly 100 μm of propagation, a bounding ellipse in this energy–position space can be fitted (not shown), oscillating and breathing in a complementary fashion to the behaviour in the transverse picture (Supplementary Video 1.) For both videos, the top panel shows the distance between pillars (observe the tapering from $z = 0$ to $z = 500$ μm, where the abrupt tall lines represent the phase jumps throughout the structure).

The complexity of the final acceleration structure is quite intricate. As the electrons gain energy in every local period (every pillar pair),

the final electron pulse at the output is dependent on the sequential parameters of the structure: tapering, and positions of the APF phase jumps. Any deviation from the structure design results in an accumulating error in the beam as it propagates throughout the structure, and can strongly affect the resulting beam parameters. Extended Data Table 1 shows the result of the optimization process in terms of macrocell parameters.

Structure fabrication

The nanophotonic accelerator structures are fabricated from n-doped (phosphorus) <100>-oriented silicon with a resistivity of 1–5 Ω cm. The initial silicon substrates approximately 2×2 cm² in size are coated with 400 nm of ma-N 2405 negative photoresist, which is subsequently patterned with a 100 kV e-beam lithography machine (Raith EBPG 5200). For development, the sample is submersed in AR 300-47 developer for 50 s. Here a slight underdevelopment is employed to leave some residue of the resist behind, which prevents parts of the mask from moving during the development process. This residue gets removed in a mild reactive ion etching process with oxygen.

A cryogenic reactive ion etching process (Oxford Instruments Plasmalab100) with sulfur hexafluoride (SF₆) and oxygen (69 and 11 standard cubic centimetres per minute, respectively) at –120 °C and 40 W radio-frequency power is used to etch the silicon to a depth of 2 μm (Extended Data Fig. 4).

The mesas (Extended Data Fig. 5) are fabricated after the accelerator structures. To fabricate the mesas, a 6-μm-thick layer of AZ 4562 photoresist is patterned using ultraviolet laser lithography (Heidelberg Instruments DWL 66+) and developed with AZ 400 K developer. A Bosch process is employed to etch the silicon surrounding the mesas to a depth of 60 μm.

In the final step, we perform a rough removal of the resist with mr-Rem 700 resist remover and remove any residue using piranha solution.

In addition to the full 500-μm structure, we also fabricated three shorter versions at 200 μm, 300 μm and 400 μm, which have the same design albeit being truncated. In this way, in experiment, the accelerated beam can be probed in these steps and the energy gain assessed. Extended Data Table 2 lists key parameters for comparing the parameters of the different structure lengths, where the measured energies often and naturally deviate from design, which takes into account only the synchronous electron, with the entire accelerated bunch oscillating around it in energy and position.

Alternating phase focusing effect on uncaptured electrons

In the main text, we mainly discuss the guiding effect of alternating phase focusing on electrons captured in the acceleration bucket. However, we can also see a similar guiding effect on electrons around the zero-loss peak (Extended Data Fig. 6 and Supplementary Video 1), which are mismatched with the structure tapering and thus cannot satisfy the synchronicity condition. The electron transmission through the structure without any laser illumination considerably decreases with structure length due to the finite beam emittance. With laser illumination, however, the beam is subject to additional transverse forces as described in the main text. Most electrons around the zero-loss peak are not captured and quickly fall off synchronicity, but surprisingly, for structures up to 400-μm long, the laser-illuminated structures show a close to three-times-higher electron transmission compared with no laser illumination. The main reason for this is the robustness of the APF effect over finite distances. This is because the electrons are close to synchronous for a large initial part of the structure (even if they are not in the acceleration phase), as the structure period increases at a slow average rate of about 16 nm per 100 μm. Therefore, although the uncaptured electrons around the zero-loss peak arrive at the phase jumps with mismatched energies, the mismatch in phase jump is still small enough such that the APF action is effective. For structures longer than that, as seen

in the case of the 500- μm -long structure, the difference in transmission between laser on and laser off vanishes almost completely because of an accumulated error in phase and gradual increase in the transverse beam size of uncaptured electrons: the conditions for APF become unstable.

Accelerated current

In our measurements, the accelerated current is fairly low due to the nature of the set-up. We use 257-nm laser pulses with a repetition rate of 167 kHz to trigger the electron emission from a modified commercial SEM electron source, not at all built for this purpose. This results in about 0.005 electrons per pulse (about 800 electrons per second) reaching the sample chamber of the SEM. With our experimental parameters, the electron pulse in the chamber is about 700 fs long compared with 250 fs (full-width at half-maximum) of laser pulse duration, where the field required for the coherent acceleration is obtained for an even smaller fraction. Our simulations predict a probability of about 3.6% of these electrons to be captured in the acceleration bucket, which holds only for the fraction of electrons interacting with the ideal laser field, that is, the part around the crest of the laser pulse envelope. With an efficiency of our microchannel plate electron detector in the range of 10–60% (ref. 49), we arrive at a rough estimate of 1 to 6 electrons accelerated and detected per second. This accelerated current does not change substantially while extending the length from, for example, 400 μm to 500 μm (Extended Data Fig. 2). But the total current passing through the structure decreases considerably due to the instability of the APF effect for non-synchronous electrons (Extended Data Fig. 6). This results in a rise in normalized current (Fig. 2) as it is normalized to the zero-loss peak height.

For almost all applications, this current is nowhere near useful but there are many avenues to increase the current by many orders of magnitude: the SEM electron source itself can emit up to 1,000 electrons per pulse; therefore, a custom electron source with a high-current and high-brightness mode could offer an up to 10^5 higher electron count, with all other parameters fixed; the repetition rate of laser pulses can at least be a factor of 10 to 100 larger, with some efforts (other structure material) probably a factor of 10,000. Even more promising is to extend the structure laterally with multiple accelerator channels next to each other providing acceleration⁴⁰ or even extending it vertically into a fully three-dimensional structure⁴¹. Furthermore, new combinations of driving wavelength and high-damage-threshold materials could also provide orders-of-magnitude gains in the maximal acceleration current as well as the acceleration gradient. Lastly, longer wavelengths allow to work with wider acceleration channel widths, facilitating the in-coupling of wider and thus higher current electron beams.

Scalability. Further scalability of this nanophotonic accelerator is an open question. When the vertical dimension is not taken into account, as can also be seen in the simulations (Extended Data Fig. 2), the number of electrons captured in the bucket remains roughly constant throughout the propagation from about 200 μm and onwards. We expect this portion to remain captured for longer structures, that is, in terms of scaling—constant for arbitrary lengths.

However, experimentally, the third dimension (vertical transverse dimension) has to be considered as a source of electron loss. Although a proposal for a full three-dimensional guiding has been put forward³¹ using side illumination, we predicted that using our current top-illumination driving scheme some form of vertical guiding is

possible³². Thus, even without specially engineered three-dimensional structures, as is the case in our current work, confinement in the vertical direction is possible although limited, and depends on the starting and final energies, and the pillars' height. A simple scaling cannot be easily defined without making too-crude approximations, and the only viable way to estimate the losses in the vertical direction is to perform Monte Carlo simulations.

For the trade-off between the overall acceleration and the number of electrons being accelerated, we do not currently have quantitative simulations. In general, however, the more electrons being accelerated, the smaller the acceleration gradient (smaller phase space available close to acceleration crest).

The accelerated flux, meaning the electrons that are in the acceleration bucket, does not decrease (at least in perfectly fabricated structures). The decrease in flux observed in Extended Data Fig. 2 is not the coherently accelerated bucket but number of electrons within $\pm 1\text{-keV}$ deviation from design energy (as mentioned in 'Structure design and optimization'). Therefore, early on, it captures non-synchronous electrons and electrons that are close to synchronous but never quite make it into the bucket. The comparison of the accelerated flux with the outgoing flux is visible in Fig. 2 as the accelerated flux is normalized to the zero-loss peak. However, in our case, this is more dependent on the experimental set-up (the laser pulse much shorter than the electron pulse and so on), than the design and physics of the accelerator itself.

Data availability

Source data for Fig. 2 are provided at <https://doi.org/10.5281/zenodo.8220588> (ref. 50).

46. Kozák, M. et al. Ultrafast scanning electron microscope applied for studying the interaction between free electrons and optical near-fields of periodic nanostructures. *J. Appl. Phys.* **124**, 1–10 (2018).
47. Dimitrov, N. et al. Pulse front tilt measurement of femtosecond laser pulses. *Opt. Commun.* **371**, 51–58 (2016).
48. Hughes, T., Veronis, G., Wootton, K. P., Joel England, R. & Fan, S. Method for computationally efficient design of dielectric laser accelerator structures. *Opt. Express* **25**, 15414 (2017).
49. Wiza, J. L. Microchannel plate detectors. *Nucl. Instrum. Methods* **162**, 587–601 (1979).
50. Chlouba, T. et al. Coherent nanophotonic electron accelerator—dataset. *Zenodo* <https://doi.org/10.5281/zenodo.8220588> (2023).

Acknowledgements We acknowledge discussions with the members of the Accelerator on a Chip International Program (ACHIP). We thank the Max Planck Institute for the Science of Light clean-room facility staff, in particular O. Lohse and F. Gannott, for continued assistance, C. McGray from Modern Microsystems Inc. for advising on fabrication methods, and Y. Tsur and N. Lindlein for discussions on the zoom lens design. We acknowledge funding by the Gordon and Betty Moore Foundation (GBMF4744 and GBMF11473), ERC Grants NearFieldAtto (616823) and AccelOnChip (884217) and BMBF projects O5K19WEB and O5K19RDE.

Author contributions S.K. and L.B. measured and analysed the data. R.S. designed the structures and performed simulations. J.L. fabricated the structures. T.C., S.K., L.B. and R.S. built the set-up. S.K. and R.S. designed and built the pulse-front-tilt set-up. T.C., R.S. and P.H. wrote the paper. P.H. supervised the experiment.

Competing interests The authors declare no competing interests.

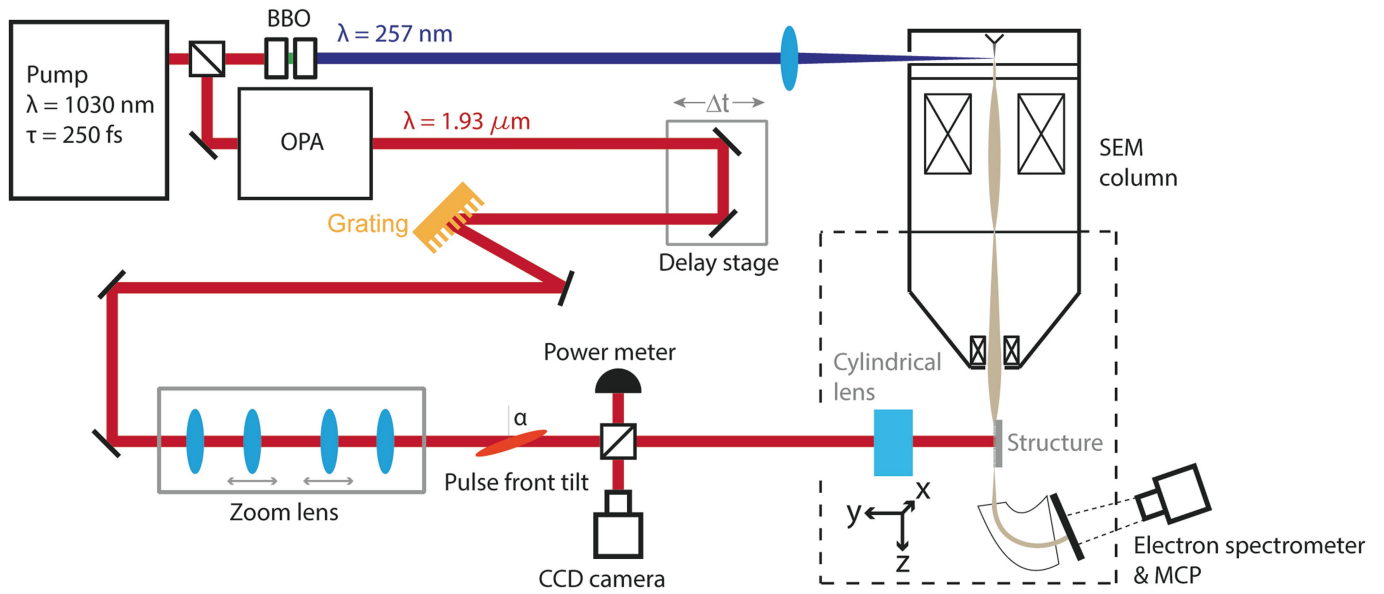
Additional information

Supplementary information The online version contains supplementary material available at <https://doi.org/10.1038/s41586-023-06602-7>.

Correspondence and requests for materials should be addressed to Tomáš Chlouba or Peter Hommelhoff.

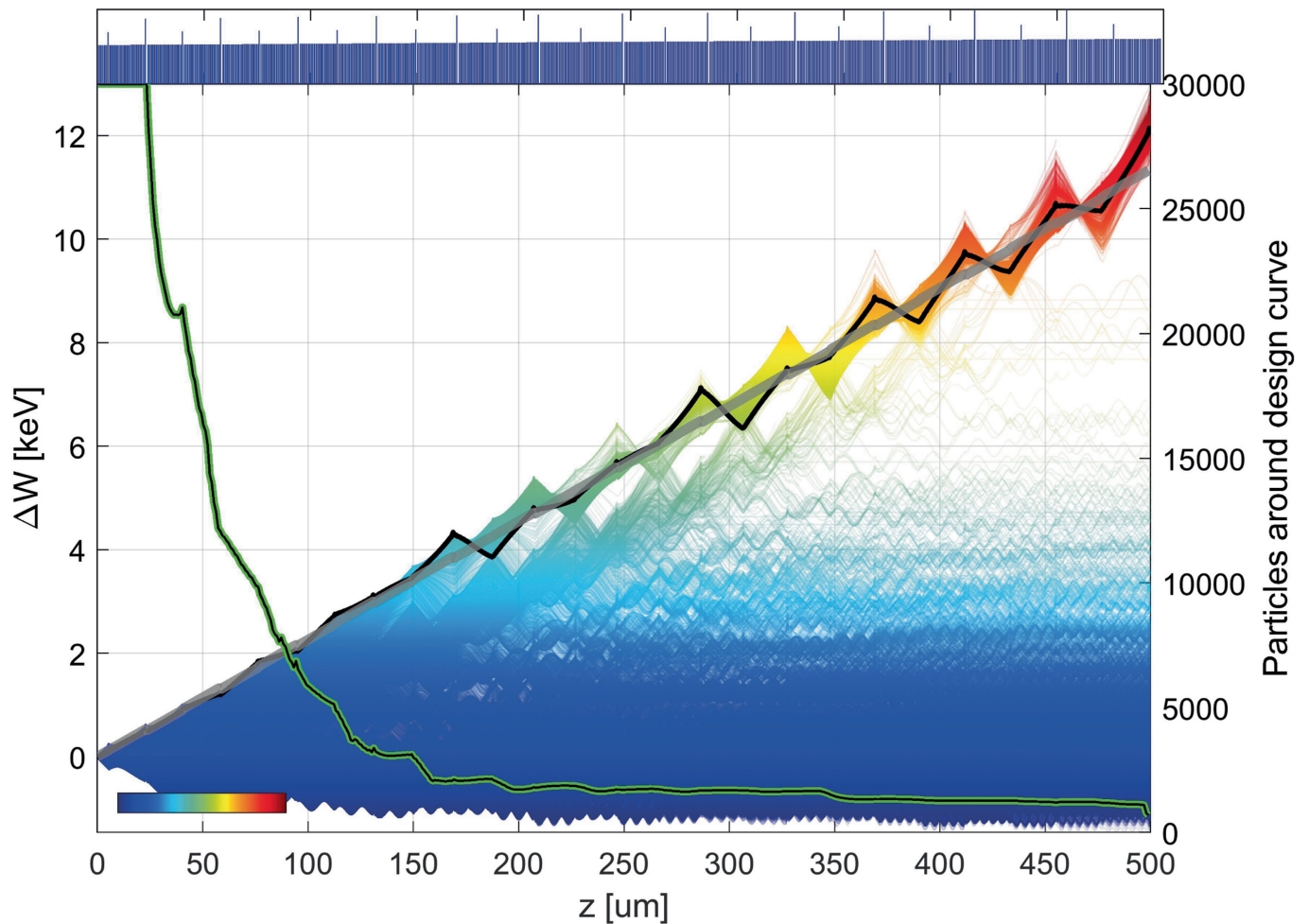
Peer review information *Nature* thanks Ido Kaminer, Yelong Wei and the other, anonymous, reviewer(s) for their contribution to the peer review of this work.

Reprints and permissions information is available at <http://www.nature.com/reprints>.



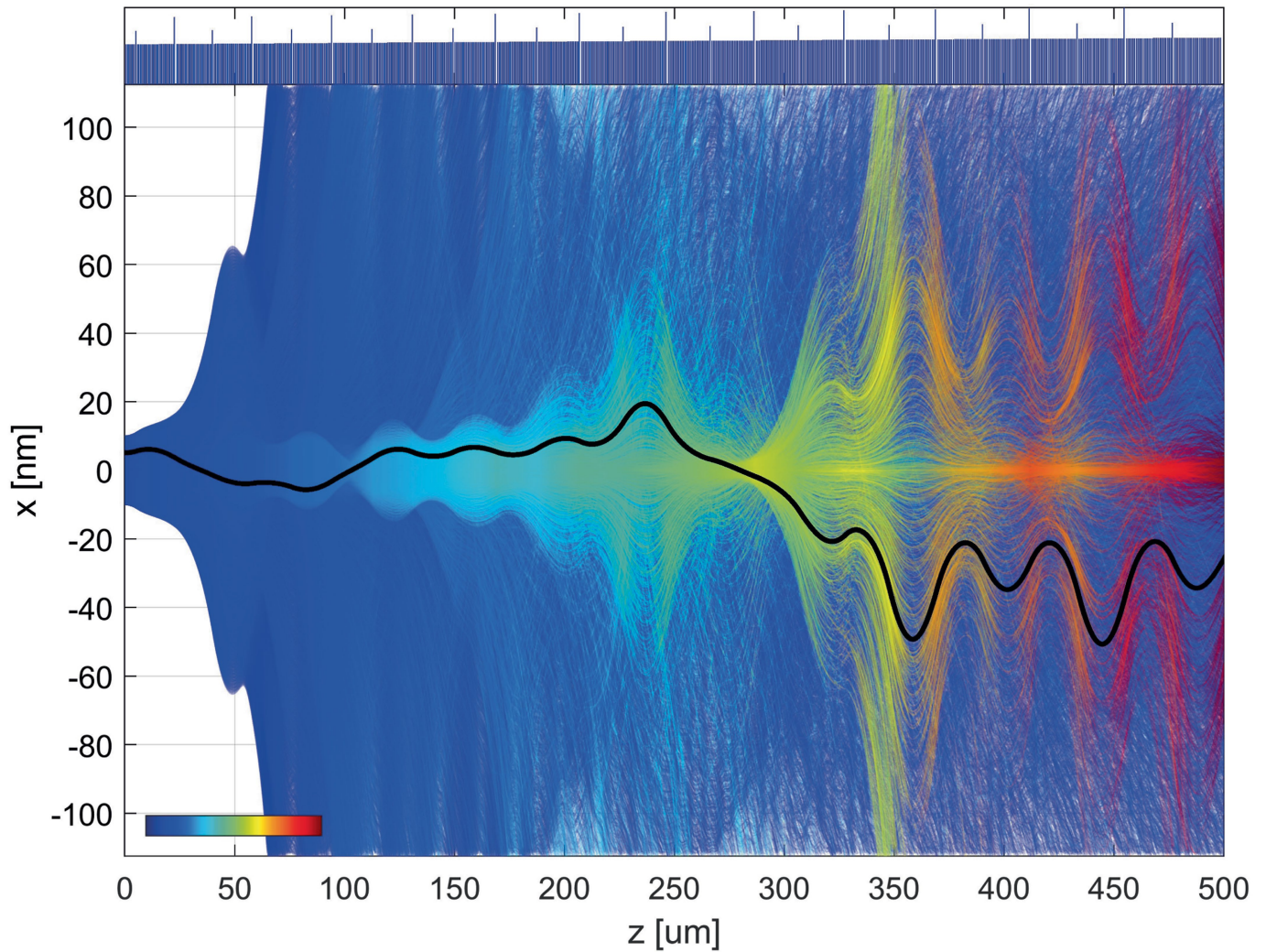
Extended Data Fig. 1 | Schematics of the experimental setup. Ultraviolet (UV) laser pulses of 257 nm wavelength (blue) and infrared (IR) laser pulses of 1.93 μm wavelength (red) are generated in an optical parametric amplifier (OPA) and fourth harmonic generation setup (two BBO crystals). The UV pulses are focused onto the SEM cathode tip to generate electron pulses that are injected into the nanophotonic structure. The IR pulses are diffracted at a grating and imaged with a cylindrical zoom lens system to generate a pulse

front tilt of $\alpha = 71^\circ$ at the structure. The pulse-front-tilted beam is focused in x-direction onto the structure with a cylindrical aspheric lens of 20 mm focal length. The time delay between IR pulses and electron pulses is adjusted with a motorized delay stage. A home-built magnetic spectrometer is used to measure the electron energy. The energy spectrum is recorded by imaging the micro-channel plate (MCP) detector screen with a camera.



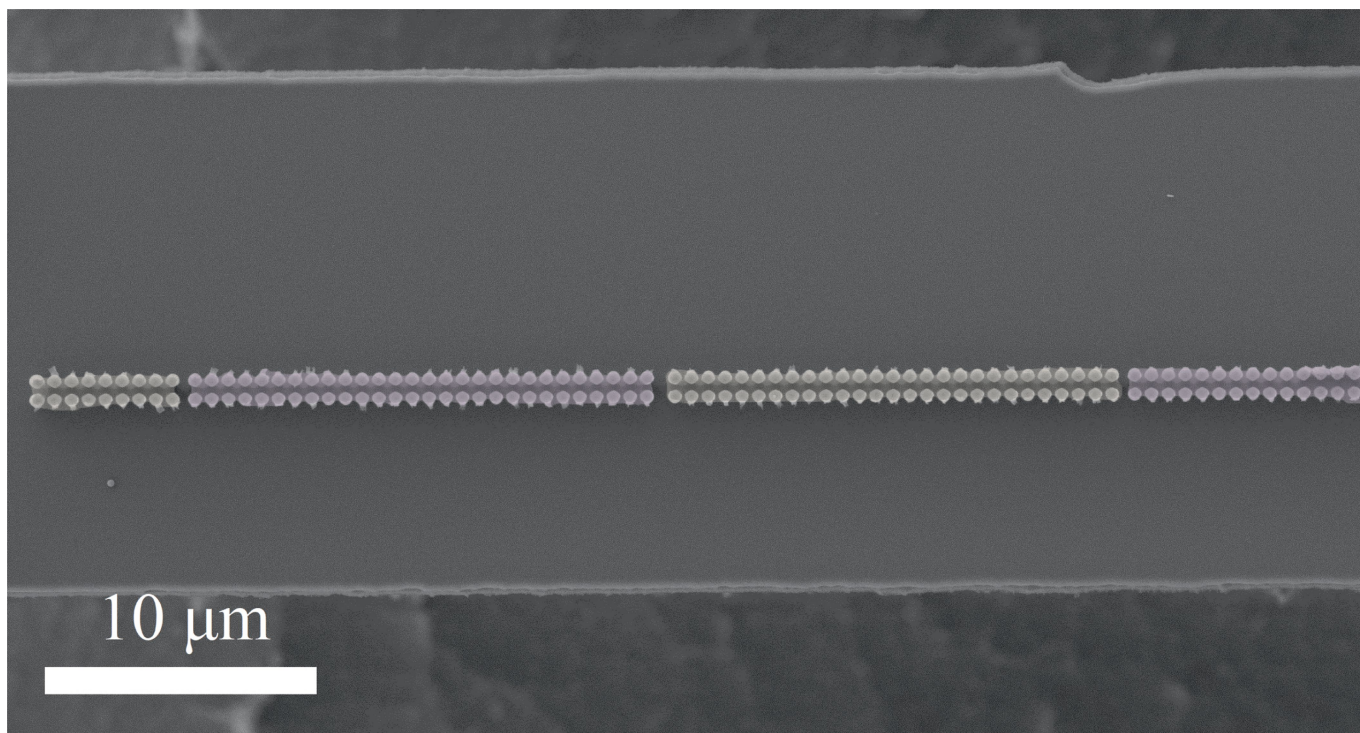
Extended Data Fig. 2 | Particle trajectories depicting energy gain vs. longitudinal dimension. The design curve (see text) is shown in grey, whereas the black curve is the particle trajectory that best matches the energy gain design curve using a least-squares fit. The colour scale indicates the energy gain from 0 (blue) up to 12.8 keV (red), as does the vertical position (left axis). The green curve shows the number of particles that follow the design curve with up to ± 1 keV deviation (the only curve in this graph referring to the right axis). Importantly, a whole number of trajectories around the main black trajectory follow closely the design curve. These trajectories reflect the particles in the coherently accelerated bucket. Below the design curve, another band of trajectories appears to follow the average gradient – these are electrons that fell off synchronicity and were captured by the next “bucket”, however, these also suffer from strong deflection forces which eventually result in loss

of most of these particles to the physical boundaries of the channel. The rest of the trajectories (mostly blue) represent electrons that quickly fell out of synchronicity and oscillate in energy. The action of the 25 APF phase jumps representing 13 APF periods is reflected in the saw tooth-like pattern. While there are sections in which the coherently accelerated particles are decelerated, they are accelerated for the most part and obviously undergo net acceleration (energy gain). The blue vertical lines in the top panel show the distance between individual pillars along the structure: the phase jumps of each APF period stand out: 120° jumps are the shorter outstanding lines, while the 240° jumps are the longer ones. Likewise, the tapering of the structure period needed to maintain synchronicity with the accelerated particles is evident from the structure input ($z = 0$) to the output ($z = 500 \mu\text{m}$) by the overall increase of the period length, i.e., the noticeable positive overall slope. See also Video 2.

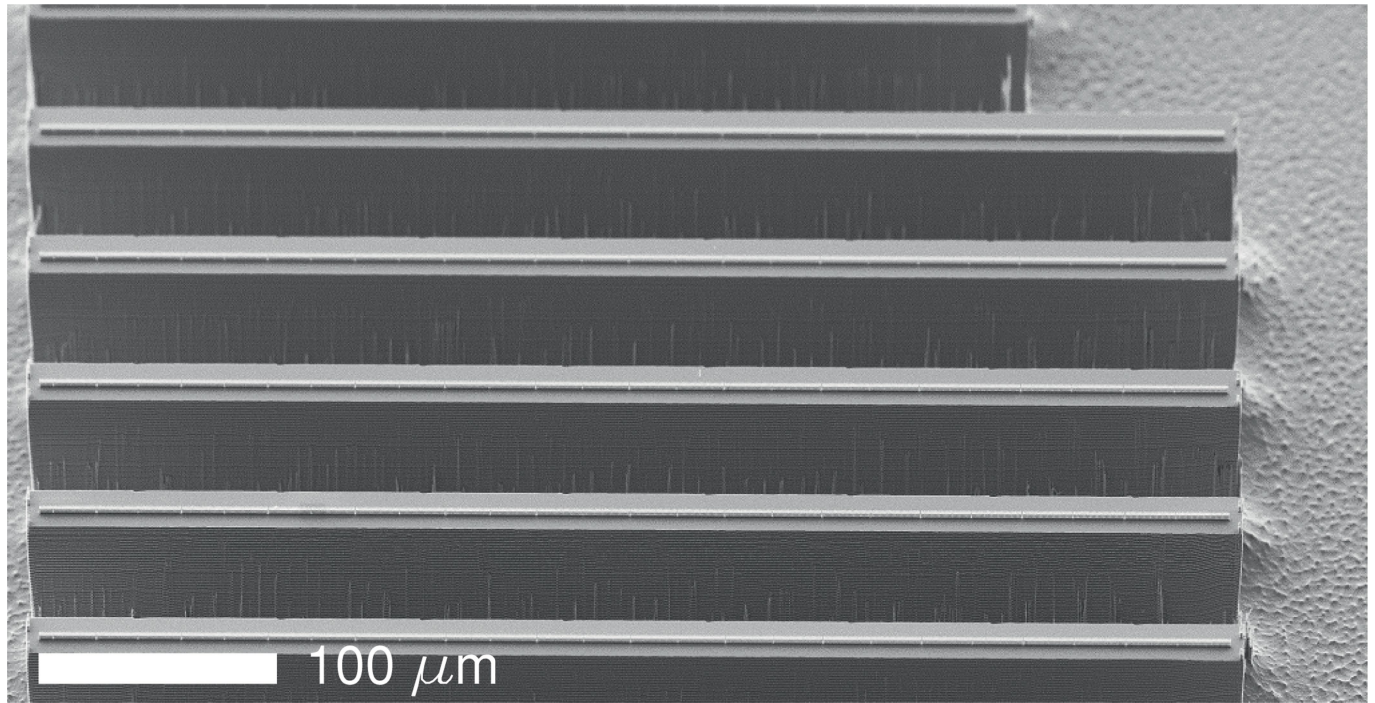


Extended Data Fig. 3 | Trajectories (transversal vs. longitudinal dimension). 30,000 electrons are uniformly distributed in time over a full laser cycle (6.45 fs) and around $x = 0$ with a full width of 20 nm. They are injected into the simulation prior to the structure, and at $z = 0$ immediately start to undergo transverse deflection due to the optical forces, along with acceleration. Only those electrons that are injected at the correct time are captured and accelerated, which, in this representation, can only be seen by the changing colour: As before, the colour indicates the instantaneous energy of the particle at a specific position (dark blue: 0 energy gain, red: 12.8 keV energy gain).

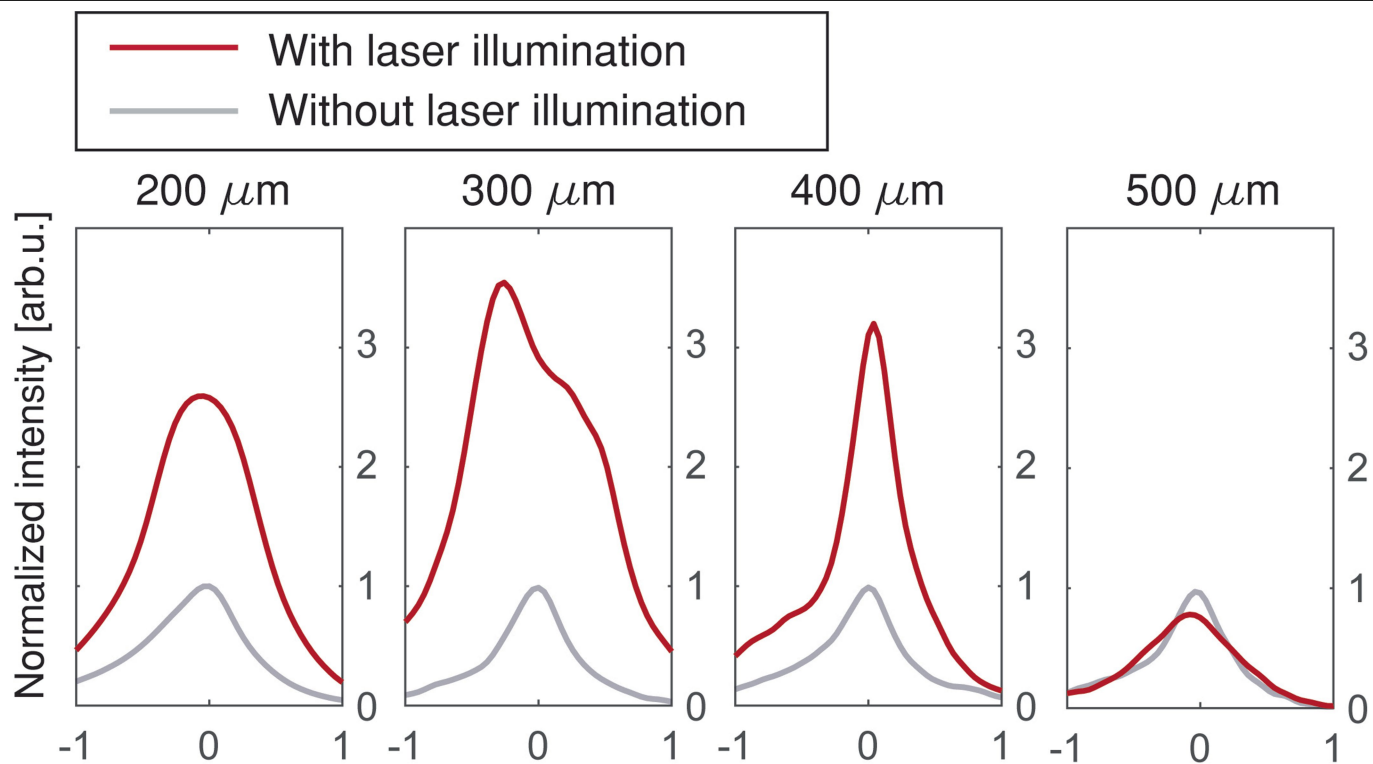
These captured electrons perform oscillations transversely in accordance with the APF phase jumps, along with complementary longitudinal oscillations (see Extended Data Fig. 2). The electrons which are not captured oscillate as well, although out of phase, and most eventually crash into the physical boundaries of the structure and are lost (at $x = \pm 112$ nm). Similar to Extended Data Fig. 2, here we mark the particle that best matches the design (black); like before, the top panel again depicts the tapering and the APF phase jumps along the structure. See also Video 1.



Extended Data Fig. 4 | SEM view of the part of the structure from top. We show a top view of the first 50 μm of the accelerator structure. Two short 120° APF jumps and a long 240° jump are clearly visible. The macrocells are slightly coloured matching the colour code of Fig. 1.



Extended Data Fig. 5 | Zoomed-out SEM view of several accelerator channels sitting on mesas. Tilted view showing an overview of mesas with accelerator structures on a chip. On each chip there are multiple structures of the same design in case one or more structures are damaged.



Extended Data Fig. 6 | Alternating phase focusing effect on uncaptured electrons. Electron spectra around the zero-loss peak for various structure lengths both with (red) and without (grey) laser illumination. Units on the horizontal axis are keV. The extra current visible for shorter structures with

laser illumination is a consequence of alternating phase focusing. The effect is less pronounced for the 400 μm structure and completely vanishes for the 500 μm structure (see text for details).

Extended Data Table 1 | Design parameters for the full 500µm structure

Macrocell #	Position [µm]	Length [µm]	Initial local period [nm]	Design energy gain [eV]	Number of pillar pairs
1	0.0	5.0	619.0	113.0	9
2	5.0	17.6	620.5	409.0	28
3	22.6	17.3	624.3	364.0	27
4	39.9	17.9	628.4	436.0	28
5	57.8	18.2	632.2	388.4	28
6	75.9	18.1	636.4	441.6	28
7	94.0	18.4	640.2	393.3	28
8	112.4	18.3	644.5	447.1	28
9	130.7	18.6	648.2	398.2	28
10	149.4	19.2	652.4	467.9	29
11	168.5	18.9	656.3	397.8	28
12	187.4	19.4	660.3	452.5	29
13	206.8	19.8	664.1	423.4	29
14	226.6	19.7	668.3	458.0	29
15	246.2	20.0	672.1	428.5	29
16	266.2	19.9	676.2	463.4	29
17	286.1	20.2	680.0	433.5	29
18	306.3	20.8	684.1	484.7	30
19	327.2	20.5	688.0	433.1	29
20	347.6	21.1	692.3	512.5	30
21	368.7	21.4	696.2	460.0	30
22	390.1	21.3	700.6	518.6	30
23	411.4	21.7	704.5	465.5	30
24	433.0	21.6	708.8	524.7	30
25	454.6	21.9	712.7	470.9	30
26	476.5	22.5	717.0	547.4	31

Includes a total of 733 pillar pairs.

Extended Data Table 2 | Key parameters of the fabricated structures

Length [μm]	Final design energy [keV]	Design energy gain [keV]	Final period [nm]	Total number of phase jumps
200	32.95	4.55	662.8	11
300	35.168	6.768	682.6	16
400	37.461	9.061	702.3	21
500	39.733	11.333	721	25

An initial electron energy is 28.4 keV (initial pillar period of 619 nm) and an average design gradient is 22.7 MeV/m.